

Main Manuscript for**Nondestructive, quantitative viability analysis of 3D tissue cultures using machine learning image segmentation**

Kylie J. Trettner^{1,2}, Jeremy Hsieh³, Weikun Xiao^{2,†}, Jerry S.H. Lee^{1,2,4}, Andrea M. Armani^{1,2*}

¹ Mork Family Department of Chemical Engineering and Materials Science, Viterbi School of Engineering, University of Southern California, Los Angeles, CA

² Ellison Institute of Technology, Los Angeles, CA

³ Pasadena Polytechnic High School, Pasadena, CA

⁴ Department of Medicine, Keck School of Medicine, University of Southern California, Los Angeles, CA

† Now located at Appia Bio, Los Angeles, CA

* Andrea M. Armani

Email: aarmani@eit.org

Author Contributions: K.J.T. performed particle synthesis, tissue culture experiments, imaging, and data analysis; K.J.T., J.H., and A.M.A conceptualized the SAAVY algorithm; J.H. created code, annotated, and trained data; K.J.T. and W.X. performed expert analysis; K.J.T., J.H., and A.M.A. wrote the manuscript; W.X. and J.S.H.L edited and approved of the final manuscript documents.

Competing Interest Statement: J.S.H.L. serves as Chief Science and Innovation Officer for Ellison Institute, LLC (paid); consultant for Henry M. Jackson Foundation (paid); scientific advisory board for AtlasXomics, Inc. and ATOM, Inc. (unpaid, travel support) outside the submitted work. A.M.A. serves as the Senior Director of Engineering and Physics for Ellison Institute, LLC (paid).

Classification: Physical Sciences; Biophysics and Computational Biology

Keywords: imaging, cellular viability, machine learning

This PDF file includes:

Main Text
Figures 1 to 4
Table 1

Abstract

Ascertaining the collective viability of cells in different cell culture conditions has typically relied on averaging colorimetric indicators and is often reported out in simple binary readouts. Recent research has combined viability assessment techniques with image-based deep-learning models to automate the characterization of cellular properties. However, further development of viability measurements to assess the continuity of possible cellular states and responses to perturbation across cell culture conditions is needed. In this work, we demonstrate an image processing algorithm for quantifying cellular viability in 3D cultures without the need for assay-based indicators. We show that our algorithm performs similarly to a pair of human experts in whole-well images over a range of days and culture matrix compositions. To demonstrate potential utility, we perform a longitudinal study investigating the impact of a known therapeutic on pancreatic cancer spheroids. Using images taken with a high content imaging system, the algorithm successfully tracks viability at the individual spheroid and whole-well level. The method we propose reduces analysis time by 97% in comparison to the experts. Because the method is independent of the microscope or imaging system used, this approach lays the foundation for accelerating progress in and for improving the robustness and reproducibility of 3D culture analysis across biological and clinical research.

Significance Statement

Cell viability is an assessment of overall culture health and is frequently used in biology and pharmacology to quantify the impact of a perturbation on a sample. Standard assays require the addition of colorimetric reagents or complete cell lysis of the culture, which limits their ability to perform continuous studies. Additionally, most methods are not optimized for use in 3D cultures that more accurately mimic *in vitro* systems. By replacing these destructive techniques with a label-free, machine learning-based image analysis method, the viability of a 3D culture can be continuously measured. This algorithm's potential in performing longitudinal investigations studying the impact of therapeutic on a 3D culture of pancreatic ductal adenocarcinoma is demonstrated.

Main Text**Introduction**

Cellular viability is a fundamental metric used to characterize the growth characteristics and proliferative capability of cell or tissue cultures. Viability assays are used throughout biology and preclinical toxicology to understand a wide range of behaviors, such as changes in cell growth induced by therapeutic perturbations or change in cell culture conditions. Assaying techniques range from colorimetric indicator dyes (1–4) or fluorescence probes (5, 6) to an analysis of the metabolic activity by chemically lysing the cells to determine the amount of ATP present using luminescence (7). Results, typically reported from 0% to 100%, are obtained by evaluating the ratio of healthy to dead cells or the metabolic activity of healthy cells in a sample

population. In some cases, cell viability assay results are supported by performing orthogonal measurements, such as sample imaging.

As the application of deep learning to image analysis has increased in the biomedical field (8, 9), many researchers have found value in automating image analysis pipelines to extract quantitative information about the cellular systems studied (10, 11). These computational models can segment and identify single cells and cell types (12–14), predict phenotypes of the cells (15, 16), assign fluorescent markers to cell images (17, 18), and quantify viability of the cells within a given image (19). The principles behind these models have enabled advances beyond single cell and apply to tissue-level analyses (20), medical imaging (21, 22), and predictive diagnostics for diseases such as cancer (23–26). However, a weakness of both the original viability assays and the imaging techniques is that they were initially developed for use in 2D culturing conditions in flasks/dishes or multi-well plate formats.

Recent research has demonstrated that cells grown in 3D culturing systems better recapitulate the matrix interactions and cell phenotypes found in physiological tissue (27). The representation of these complex interactions provides an improved *in vitro* method for compound screening over 2D systems. While improvements in imaging technology have advanced the ability to capture qualitative information about 3D cell models and tissues (28–30), the need for longitudinal quantitative assessment of culture viability is still present. Various strategies are being pursued to address this challenge. One manufacturer has adapted their assay to create a 3D culture specific product. This product is called CellTiter-Glo 3D (CTG) and has quickly become an industry standard assay used to report viability by measuring the metabolic activity of the culture. However, the CTG development procedure requires complete cell lysis. For other methods, researchers have investigated the comparative use of previously developed assays (4) and recommend complementary imaging for experiments utilizing 2D specific reagents to cross reference results (31). Although the field has begun adapting viability assays (32–34) and deep learning techniques to the dynamic nature of 3D systems (35, 36), quantification of viability largely requires additional experimental steps for fluorescently labeling the culture system (37, 38) or developing metabolic assays (39, 40). This remaining challenge provides a unique opportunity to utilize deep learning to augment 3D viability assays.

In the present work, we develop and validate a Segmentation Algorithm to Assess the Viability (SAAVY) of 3D cultures. We designed SAAVY to automatically identify and analyze the critical orthogonal features in spheroid and organoid structure that experts correlate with cellular viability, such as the transparency of the spheroid and the overall morphology. We ensure that SAAVY can withstand a degree of background noise as we wanted to account for common defects, such as dead cell fragments or matrix particulate deposits, that may be present in 3D cultures. SAAVY was trained and tested against clear and noisy backgrounds to achieve noise tolerance. SAAVY calculates the viability of each uniquely identified spheroid in an image and an overall average viability for all 3D structures present in a well. It also reports total spheroid count per image, spheroid radius, spheroid area, and other metrics of relevance. The total analysis time per well is approximately 0.3 seconds. This type of integrated analysis provides insight into a biological system's response at both the individual spheroid and entire well level. Lastly, SAAVY is agnostic of microscope system or manufacturer and does not require fluorescent or colorimetric indicators, enabling longitudinal studies to be performed.

After validating the accuracy of SAAVY in analyzing pancreatic ductal adenocarcinoma (PDAC) spheroids in clear and noisy backgrounds through a blinded comparison with a pair of experts, a series of application-driven experiments were conducted. We first compared SAAVY analysis with an industry standard metabolic assay for 3D cultures, including expert analysis as ground truth. To challenge SAAVY's ability to detect nuanced changes in response to a

perturbation, we then performed a label-free imaging-based longitudinal study investigating the effect of an FDA-approved therapeutic on the pancreatic cancer spheroids.

Results and Discussion

To segment the biological regions of interest in an image, prior image recognition approaches focused on utilizing relatively simple edge detection techniques to identify spheroid boundaries (41, 42). However, edge detection with watershed has poor reliability when spheroids or organoids overlap or when background noise is present, limiting the utility to images with low spheroid density or complete separation of cell colonies (40). Other characterization workflows reduced or eliminated this overlap by altering culturing conditions (e.g. growing single spheroids per well) or image acquisition settings (e.g. increased magnification on the sample wells to obtain one spheroid per image) on a case-by-case basis (40, 41, 43). This bespoke approach relies on image-stitching and partial data rejection of overlapping regions of interest, which can lead to unintentional bias in the final data set (44, 45). Our goal is to develop an algorithm that can analyze an image of an entire well with minimal data rejection while resisting the influence of background noise, which requires a different approach to segmentation.

As a proof of concept, pancreatic ductal adenocarcinoma (PDAC) spheroid samples are used. PDAC spheroids are of a cystic phenotype and tend to grow randomly throughout the well (46). This growth pattern leads to a high frequency of overlapping cell structures and makes them difficult to analyze using edge detection machine-learning approaches. Healthy cystic spheroids are distinguished by their open lumen and transparent centers with distinct, circular edges when viewed in plane. The transparency and circular morphology of healthy spheroids are in stark contrast with the opaque, blebbled spheroids that characterize dead spheroids of this type. This correlation between transparency and morphology in brightfield images has been previously studied (47, 48). The expansion of this correlation to cellular state is what motivated our image-based intensity quantification approach.

SAAVY design

An overview of SAAVY is presented in Figure 1 and details are included in the SI. SAAVY is first created by fine-tuning a pre-trained Mask R-CNN model in PyTorch (49). This implementation is particularly attractive due to its improved ability to separate overlapping features. This transfer learning approach reduced the total cost for bespoke images of cystic spheroids and allowed us to move forward with a relatively small number of expert-annotated images (50). We further refined our model with a balanced dataset consisting of 24 images of PDAC spheroids with clear and noisy backgrounds that spanned the entire viability range.

SAAVY analyzes brightfield, label-free images of tissue culture spheroids by segmenting each individual spheroid and outlining the identified region on the output image. Subsequently, SAAVY quantifies the viability of each uniquely identified spheroid using the average intensity of the segmented region compared to the background using a weighted average model as detailed in the Supplementary Information. This approach allows for an increased level of background noise to be present without negatively impacting the assessment ability. Several other metrics are calculated by SAAVY including the average viability, the average spheroid size and total spheroid count across each image. With our hardware configuration, each image required 0.3 seconds for the entire analysis process. While viability assessments of 3D cultures are routinely performed as a quality check during experimentation by experts, the single-spheroid level quantitative analysis across an entire well is not easily obtained from expert analysis and is not possible using biochemical measurements. Therefore, SAAVY provides several orthogonal dimensions for analytics on an accelerated timescale.

The initial training and validation data set contains a series of label-free microscopy images of PDAC spheroids cultured either in a clear or a noisy culture matrix. The noisy matrix was created by intercalating opaque nanoparticles throughout the gel. Images are acquired at days 0, 4, and 6 of spheroid growth at 5x magnification, and each image captures the entire 10

μ L gel seeded in a 96-well plate. The resultant data set contains 1,328 widefield images. Notably, no images or wells were rejected from the data set. Additional experimental details are included in the SI.

Representative examples of SAAVY-analyzed images across all days and both clear and noisy backgrounds are presented in Figure 2. Both the original and the analyzed images are shown. As can be seen, SAAVY is able to identify spheroids in the presence of potential confounds and in cases where spheroids are overlapping. Notably, the entire image was analyzed at once. In total, SAAVY detected and provided information about 10,158 unique spheroids across the 1,328 images.

SAAVY to Expert comparison

SAAVY performance was evaluated as compared to a pair of blinded experts for the entire image population of clear and noisy background gels. The justification for expert selection and the blinding method is detailed in the SI. The quantification of distribution differences was first calculated to understand the similarities of SAAVY to each expert. For this quantification, Earth Mover's Distance (EMD) was used (51). Values of 0 correspond to less distance between the distributions, or classically that the effort is minimized to transform one distribution into the other. The EMD values are represented by the 'Similarity' row in Table 1. Further, the reliability was quantified using Krippendorff's alpha, a measure of inter-rater reliability. Values close to 1 suggest perfect reliability whereas values closer to zero and negative values suggest poor reliability and systemic differences, respectively. The supplemental information contains a comparison of other common metrics and data correlations that we calculated and compared for this analysis.

The EMD values are highest on Day 0, regardless of background, suggesting dissimilar distributions as compared to Days 4 and 6 of the analyzed images. The reliability data supports this finding, and it is negative for both experts in both background conditions. This result is potentially due to the presence of small bubbles in some images in this data subset. These bubbles often resemble spheroids with a circular morphology and darkened outer shell compared to the background, and SAAVY frequently identifies such defects as spheroids in subsequent analysis. However, these defects typically disappear as the gel settles and, if incurred during mixing the solution, are usually only present the day or two following seeding.

Similarity between expert and SAAVY distributions improves on Days 4 and 6. On Day 4, SAAVY shows a decrease in reliability compared to Expert 2 in clear samples. The same is not true for SAAVY as compared to Expert 1 in clear backgrounds, and the reliability is improved for both experts for noisy background gels. The similarity also follows this trend for Day 4. On Day 6, SAAVY is nearly equally reliable when comparing to both experts for both background types. However, the SAAVY distribution is more like experts for noisy backgrounds as compared to clear backgrounds. The distributions are visualized for all permutations in the SI for further comparison.

Two classifiers in the performance of SAAVY are evaluated: spheroid/no spheroid identification (ID) and live/dead detection (LD). ID is characterized as SAAVY assigning the appropriate value to each image according to the absence (value of -1) or presence (values of zero and above) of spheroids in the image. LD is characterized as SAAVY assigning viability values that correlate to live (>0%) or dead (0%) spheroids. This corresponds to the typical binary interpretation of other viability assays to keep analysis consistent with previous research. For Day 0, biological timescale is used as ground truth. Because insufficient time has passed for single-cell spheroid fragments to self-assemble into the spheroid structure, all images are deemed to have no spheroids (or "none detected"). Thus, the accuracy of this ID is calculated to quantify the performance of both SAAVY and the experts. On Days 4 and 6, ground truth was determined by Expert 1, and the details for this decision are included in the Supplemental Information. Both ID and LD performance are quantified using the F1-score and summarized in Table 2.

On Day 0, Expert 1 is 98.6% accurate at identifying spheroid absence, whereas SAAVY is only 47.1% accurate. Expert 2 was 0% accurate on Day 0, which was due to the assignment of 0% viability instead of noting no spheroids had formed with a value of -1. Days 4 showed clear improvement for both experts and SAAVY with F1-scores of 1.0 for both ID and LD analyses,

which suggests perfect agreement with the ground truth. When spheroids are observed after the given time for growth, they are distinguishable from the background. The fact that SAAVY matches experts at this task suggests that the algorithm can successfully identify and analyze spheroids in clear backgrounds comparably well to human experts. LD analysis matched this trend of perfect F1-scores (1.0) for both SAAVY and Expert on Day 4. For noisy backgrounds, the same holds true though the F1-score decreases slightly to 0.992. Day 6 is when differences between SAAVY performance and the experts begin to appear. Notably, SAAVY outperforms Expert 2 as compared to ground truth for spheroid identification. For LD analysis on clear backgrounds, it is 0.91 for Expert 2 compared to 0.89 for SAAVY. On noisy backgrounds, this is further improved to 0.96 for Expert 2 and 0.95 for SAAVY.

Although SAAVY has slightly lower F1 scores than Expert 2 for live/dead performance, this is likely an artifact related to the size of detectable viability differences characteristic to the different experts. SAAVY assigned viability values to a one-tenth of a percent as a direct scaling of the viability per pixel is 0.4%. Additionally, as can be seen in Figure SI-6, SAAVY did not exhibit a bias in assignments towards any viability range. In contrast, Expert 1 tended to estimate in 5% increments, and Expert 2 tended to estimate in 10% increments, suggesting that any image with an average viability below 5% or 10%, respective to the expert, was classified as dead. Therefore, SAAVY may classify an image of spheroids as alive although they are noted dead by experts due to its improved incrementation. To test this hypothesis, a ROC threshold analysis was completed to evaluate the level at which the threshold for live or dead can be raised to while optimizing the F1-score for SAAVY in clear samples. The threshold for SAAVY can be raised to 2.43% for clear backgrounds leading to an F1-score of 0.91, which matches Expert viability prediction while maintaining improved resolution.

Comparison against industry standard viability assay

CellTiter-Glo (CTG) is a metabolic viability assay that has been adapted and optimized for use when analyzing 3D tissue culture systems (39, 40). CTG correlates cellular ATP to the intensity of the luminescent signal measured from lysed cells. These assays are evaluated on a well-by-well basis through normalization of the well signal to positive and background control measurements. Due to well-by-well differences in cellular growth and in the cellular self-assembly process, there can be significant variations in the overall 3D culture evaluated between each well, even if the same initial cell concentration was seeded. This variation can lead to errors in the normalization process standard for reporting the results of this assay. These variations exist between wells of an assay and may limit the interpretation of CTG to a relative comparison within the same assay plate and not across assay plates. We designed a non-inferiority study to test that SAAVY would do no worse than the CTG method at characterizing viability. PDAC samples grown in either clear or noisy matrices were analyzed by the experts, CTG, and SAAVY. This approach resulted in 501 images with matched CTG data.

Without noise in the matrix, the CTG viability reading exceeded 100% a total of seventeen times (24.3% of the measurements). Once matrix impurities were introduced, the CTG viability reading exceeded 100% in 39 samples (57.4% of the measurements). It should be noted that prior research has shown an increase in metabolic activity when grown in similar nanoparticle matrices (52), so the CTG results agree with prior findings.

We compared CTG to SAAVY using Pearson's correlation, Earth Mover's distance for similarity, and Krippendorff's alpha for rater reliability across Day 6 data for clear and noisy backgrounds. Figure 3 summarizes the results of these comparisons. SAAVY and CTG have similar distributions for clear and noisy background types with EMD values of 0.023 and 0.010, respectively. We believe this agreement is due to the absence of spheroids in some images in this dataset, as the noisy background either obscured detection or killed the growing spheroids by this day. Figure SI-7 includes a histogram breakdown of this data to visualize the distributions. The reliability analysis, however, suggests that CTG is a more reliable rater on clear gels (k -alpha, 0.384) compared to noisy (k -alpha 0.076).

We could not complete a confusion matrix comparison for SAAVY and CTG because CTG cannot produce a negative result. We perform a threshold analysis on CTG to determine

what the viability percent could be raised to with the goal of enhancing the overall performance of the CTG test. However, because of the inability of CTG to provide negative (0% viable by LD analysis) measurements, we looked to a metric other than F1-score during our threshold analysis. Youden's J-statistic was used to determine that the cutoff for CTG can be raised to 18.00% and 48.15% for clear and noisy backgrounds, respectively. This suggests that the CTG assay is not specific when capturing cell state characteristics and the potential impact of an image-based companion for viability measurement.

Non-destructive tracking of perturbation longitudinal impact on 3D cultures

One current hurdle in longitudinal studies using high-throughput, automated 3D culture methods is the requirement of labeling the sample to assess viability. A non-destructive, label-free approach would allow continuous monitoring of the same spheroid, increasing research rigor and allow primary cells and samples to be used. As a step in this direction, SAAVY's ability to longitudinally track PDAC spheroid growth within the same sample is demonstrated by analyzing label-free images and creating a viability response curve.

An Operetta CLS high content imager is used to automate the image acquisition process. The longitudinal data set included 12,528 images where 406 images were randomly selected for analysis (16,214 spheroids). Imaging parameters for this assay were set on the first day and used as the standard operating protocol across the entire experiment. Important parameters to note are the z-plane within the gels (320 μ m) and the z-distance between focal planes (20 μ m). The z height was located at the mid-plane in the well. Gemcitabine, an anti-metabolite therapeutic commonly used to treat pancreatic cancer, was used for compound perturbation at concentrations of 1, 5, 10, 15, and 20 μ M. We included wells of untreated PDAC spheroids for a positive control. Treatment was added after imaging on day 4 to all wells using appropriate volumes of a stock 100 μ M solution of gemcitabine in DMSO.

The viability of the wells, plotted by treatment group, is presented in Figure 4a. Critically, we did not normalize the reported viabilities in this plot and used the raw output from SAAVY to emphasize the low error within repeated sample conditions. The decreased viabilities reported by SAAVY on Days 1 and 2 is likely due to the smaller size of the spheroids at this time, specifically taking into consideration that our training was done on Day 4 and Day 6 spheroids. However, the stability of viability across Days 3 and 4 of spheroid growth is suggestive of the overall reliability of SAAVY to track samples across different days.

SAAVY detects viability responses across all sample groups. The untreated and 1 μ M groups trend similarly for viability across all days. Interestingly, the mechanisms of compound diffusion are potentially identified in our image-based assay as well. We note a delayed spheroid-death response from the 5 μ M concentration, perhaps due to diffusion time through the gel leading to decreased availability of compound 24-hours after treatment compared to 48-hours post-treat. In contrast, we see increased viability in the 15 and 20 μ M concentrations. Upon review of the images, we found a distinctly different morphology of the spheroids. Spheroids at these higher compound concentrations look like they have collapsed on themselves, compared to the lower (5 and 10 μ M) where the spheroid looks like it has exploded and has characteristic blebbled edges suggesting cell apoptosis (as shown in the D5 and D6 images in Figure 4).

We further investigate if the decreased viability trends with spheroid area, as we expect the area to decrease as the spheroids die. This is confirmed by visualizing the average area across each of the assay, seen in Figure 4b. We see an upward trend in spheroid growth across all treatment groups through Day 4 of the assay. This metric allows us to investigate further trends in spheroid response to compound treatments. For the control group, we see continued growth through the final day of imaging. We see an expected decrease in spheroid size from Day 4 to Day 6 in the 5, 10, 15 and 20 μ M treatment groups that match the decreased viability seen on these days. For the lowest concentrations of treatment, the size increases until Day 5, though at a slightly lesser rate than the control group, where it then stays constant between Day 5 and Day 6. When taken into context with the viability data, this suggests that this concentration of compound may be enough to stall continued growth without eradicating the tumor cells. A

potential rate-based result underscores the important role that image-based surveillance methods play during cell viability experiments.

Conclusions

We develop and validate a method to quantitate viability of 3D tissue cultures in a label-free, non-destructive, and longitudinal manner that easily integrates into existing tissue culture imaging procedures. We showed comparable quantification using our algorithm, SAAVY, to human expert estimation in both clear and noisy background hydrogels with high tolerance to noise. We found improvements in classification ability and sensitivity over standard CTG assay measurement. Further, we showed the ability of SAAVY to longitudinally track 3D spheroid growth and viability for both untreated and therapeutically treated spheroids. Our algorithm uses the same principle that human experts use to evaluate images yet streamlines the process by automation. This facilitates integration of our viability method into standard tissue culture procedures in a robust and time-independent manner. The ability of our algorithm to output results of “no spheroid” as well as quantitative morphological metrics when analyzing 3D tissue culture constructs adds another classification level on top of typical live/dead classification and can provide more information to an experimentalist regarding growth characteristics of a sample.

With the augmentation of biomedical imaging with computer vision and other CNN approaches, it is possible to further develop label-free imaging methods. Our system only covered the supervised training of one tissue spheroid type, PDAC. The open-source nature of our algorithm may allow for user-specified training of different kinds of 3D spheroid culture images as well as tunability of the viability algorithm to suit the characteristics of other cultures. There is opportunity to expand the training data of SAAVY beyond one-spheroid type and utilize other deep-learning methods, such as unsupervised learning, to expand the capabilities of SAAVY. This work considered the plane of best representation of each imaged spheroid in the experimental plates. However, microscope z-stack imaging enables full 3D imaging of the tissue constructs. To truly evaluate efficacy of compounds and materials, it is important to utilize the full reconstructive capabilities when merging 3D imaging with deep learning. The ability to study fully 3D cultures may support drug discovery in uncovering how a drug affects overall growth dynamics, as the area analysis in this study suggests and other research points toward the importance of (53). In this context, improved monitoring may provide further insight to disease treatment and improve rigor in its ability to compare across experiments. The time-agnostic and non-destructive manner of this algorithm quantifies the qualities that researchers often judge when monitoring their culture. With further expansion of our training dataset to include various disease types and 3D tissue culture systems, we believe that SAAVY may prove a useful tool for real-time analysis and can complement any image-based 3D culture assay where viability must be assured.

Materials and Methods

Tissue culture

Mouse-derived pancreatic cancer (PDAC) spheroids (line 8-14F-7: KRAS G12D, PTEN loss, COX2 overexpression, female, 2 weeks old at the time of sacrifice). Pancreatic cancer spheroids were cultured using an established protocol (54) included in the Supplemental Information (SI 1.2.2). For samples that do not include any nanoparticles, the cell-laden hydrogel solution was plated in 10 μ L increments in the center of the wells on an opaque-walled 96-well plate (Corning). For samples that included nanoparticles, nanoparticle solutions were combined with cell-laden solutions to the desired concentration of cells and nanoparticles then plated in the same manner mentioned above.

Images were taken of all seeded wells on the day of seeding (Day 0, D0). The plates were left to incubate until day 4 (D4) where negative control wells were treated with 10 μ M

gemcitabine added to the cell media and images were captured of all wells. We incubated the plates for an additional two days until day 6 (D6) where we took final images of all then performed a 3D CellTiter Glo (CTG) assay (Promega) to measure the metabolic activity of the spheroids grown in each condition. CTG was performed according to the documented protocol provided by Promega and read using a BioTex plate reader for luminescent detection at 560nm. Dose-response assays were plated in the same manner described above and imaged at 320 μ m above the bottom of the well plate for consistent cross sections across all six days of experimental growth. Images were exported from the Operetta CLS microscope with a brightfield correction factor applied to images to reduce vignetting from background light within the imaged gel.

Image datasets

Our datasets include brightfield images taken during various experiments, as noted in the tissue culture methods section above. PDAC images were taken on an ECHO Revolve or Operetta CLS with 5x/0.16 objective lens. ECHO images were saved and exported in TIFF format. Images from CLS were exported as PNG. Both were converted to JPG and digitally resized to 1024x1024 for SAAVY viability analysis. The complete PDAC set included 1,328 images. Of these, 24 images were randomly selected for training, and 416 images were used for the experimental viability estimations where 135 were CTG matched. The longitudinal data set included 12,528 images where 406 were selected for analysis.

Data training, pre-processing, and final run time

We first train SAAVY using a pre-existing image set from MS COCO pretrained general model for transfer learning. We trained for 20 epochs. Based on analysis, we used the 15th checkpoint for image production due to continuous loss after this point (Figure SI-2). Using the training dataset detailed above, we annotate the 24 training images using VIA Image Annotator (2.0.11, Oxford) to specifically identify cell spheroids. Total computational time for SAAVY on the 416-image set is 2 minutes and 5 seconds (running an RTX 3080 and Intel Core i9-10850K stock).

Post-hoc analysis

We assess confusion matrices for two classifications: spheroid/no spheroid and live/dead detection. Accuracy and F1-score (SI, EQ-2,3) were calculated where appropriate to get an overview of the performance of SAAVY as compared to experts and how the experts compare to each other. We assessed data matching by first converting data to their respective probability density function and then calculating the multiple distance metrics to assess the distances between all viability estimation methods (Table SI-2).

Before performing any statistical analyses, we assessed overall normality of the data according to the group analyzed. Where appropriate, non-normal data was estimated normal according to the central limit theorem and the appropriate groupwise analyses were applied (either repeated measured analysis of variance with Tukey post hoc test or related t-test for normal data or Wilcoxon for nonparametric data from small samples). All analysis was completed in Python with the appropriate libraries noted in the SI.

Data sharing and availability

All code, training material, validation images, and Python environments are available at <https://github.com/armanilab/SAAVY>. All images from each dataset are uploaded to Zenodo (10.5281/zenodo.10086367) along with raw and complied datasets for running the associated analysis code.

Acknowledgments

We would like to acknowledge and thank the Hill Lab for PDAC spheroid culture access and training for use. Further, we extend our gratitude to Naim Matasci, PhD, the Computational Team

and Cell Line Team of the Ellison Institute of Technology for their discussions regarding analysis methods, cell growth standardization, and best procedures throughout the experimental and analysis phases of this manuscript's preparation.

The authors would like to thank the Office of Naval Research (N00014-22-1-2466, N00014-21-1-2048), National Science Foundation (DBI-2222206), and the Ellison Institute of Technology for funding this work.

Disclaimer: The contents of this publication are the sole responsibility of the authors and do not necessarily reflect the views, opinions, or policies of the USUHS, the Henry M. Jackson Foundation for Advancement of Military Medicine, Inc., the Department of Defense, the Department of the Army, Navy, or Air Force. Mention of trade names, commercial products, or organization does not imply endorsement by the U.S. Government.

References

1. G. Repetto, A. del Peso, J. L. Zurita, Neutral red uptake assay for the estimation of cell viability/cytotoxicity. *Nat. Protoc.* **3**, 1125–1131 (2008).
2. J. van Meerloo, G. J. L. Kaspers, J. Cloos, Cell sensitivity assays: the MTT assay. *Methods Mol. Biol.* **731**, 237–245 (2011).
3. P. Kumar, A. Nagarajan, P. D. Uchil, Analysis of cell viability by the lactate dehydrogenase assay. *Cold Spring Harb. Protoc.* **2018** (2018).
4. F. Piccinini, A. Tesei, C. Arienti, A. Bevilacqua, Cell counting and viability assessment of 2D and 3D cell cultures: expected reliability of the trypan blue assay. *Biol. Proced. Online* **19**, 8 (2017).
5. M. Tian, Y. Ma, W. Lin, Fluorescent probes for the visualization of cell viability. *Acc. Chem. Res.* **52**, 2147–2157 (2019).
6. J. O'Brien, I. Wilson, T. Orton, F. Pognan, Investigation of the Alamar Blue (resazurin) fluorescent dye for the assessment of mammalian cell cytotoxicity. *Eur. J. Biochem.* **267**, 5421–5426 (2000).
7. T. L. Riss, R. A. Moravec, A. L. Niles, Cytotoxicity testing: measuring viable cells, dead cells, and detecting mechanism of cell death. *Methods Mol. Biol.* **740**, 103–114 (2011).
8. F. Isensee, P. F. Jaeger, S. A. A. Kohl, J. Petersen, K. H. Maier-Hein, nnU-Net: a self-configuring method for deep learning-based biomedical image segmentation. *Nat. Methods* **18**, 203–211 (2021).
9. Y. LeCun, Y. Bengio, G. Hinton, Deep learning. *Nature* **521**, 436–444 (2015).
10. E. Moen, *et al.*, Deep learning for cellular image analysis. *Nat. Methods* **16**, 1233–1246 (2019).
11. D. A. Van Valen, *et al.*, Deep Learning Automates the Quantitative Analysis of Individual Cells in Live-Cell Imaging Experiments. *PLoS Comput. Biol.* **12**, e1005177 (2016).
12. C. Stringer, T. Wang, M. Michaelos, M. Pachitariu, Cellpose: a generalist algorithm for cellular segmentation. *Nat. Methods* **18**, 100–106 (2021).
13. M. Y. Lee, *et al.*, CellSeg: a robust, pre-trained nucleus segmentation and pixel quantification software for highly multiplexed fluorescence images. *BMC Bioinformatics* **23**, 46 (2022).

14. A. E. Carpenter, *et al.*, CellProfiler: image analysis software for identifying and quantifying cell phenotypes. *Genome Biol.* **7**, R100 (2006).
15. C. Piansaddhayanon, *et al.*, Label-free tumor cells classification using deep learning and high-content imaging. *Sci. Data* **10**, 570 (2023).
16. T. R. Jones, *et al.*, Scoring diverse cellular morphologies in image-based screens with iterative feedback and machine learning. *Proc Natl Acad Sci USA* **106**, 1826–1831 (2009).
17. E. M. Christiansen, *et al.*, In silico labeling: predicting fluorescent labels in unlabeled images. *Cell* **173**, 792–803.e19 (2018).
18. C. Ounkomol, S. Seshamani, M. M. Maleckar, F. Collman, G. R. Johnson, Label-free prediction of three-dimensional fluorescence images from transmitted-light microscopy. *Nat. Methods* **15**, 917–920 (2018).
19. C. Hu, *et al.*, Live-dead assay on unlabeled cells using phase imaging with computational specificity. *Nat. Commun.* **13**, 713 (2022).
20. N. F. Greenwald, *et al.*, Whole-cell segmentation of tissue images with human-level performance using large-scale data annotation and deep learning. *Nat. Biotechnol.* **40**, 555–565 (2022).
21. F. Milletari, N. Navab, S.-A. Ahmadi, V-Net: Fully Convolutional Neural Networks for Volumetric Medical Image Segmentation in *2016 Fourth International Conference on 3D Vision (3DV)*, (IEEE, 2016), pp. 565–571.
22. A. Casamitjana, M. Catà, I. Sánchez, M. Combalia, V. Vilaplana, “Cascaded V-Net Using ROI Masks for Brain Tumor Segmentation” in *Brainlesion: Glioma, Multiple Sclerosis, Stroke and Traumatic Brain Injuries: Third International Workshop, BrainLes 2017, Held in Conjunction with MICCAI 2017, Quebec City, QC, Canada, September 14, 2017, Revised Selected Papers*, Lecture notes in computer science., A. Crimi, S. Bakas, H. Kuijf, B. Menze, M. Reyes, Eds. (Springer International Publishing, 2018), pp. 381–391.
23. P. Mobadersany, *et al.*, Predicting cancer outcomes from histology and genomics using convolutional networks. *Proc Natl Acad Sci USA* **115**, E2970–E2979 (2018).
24. E. Wulczyn, *et al.*, Deep learning-based survival prediction for multiple cancer types using histopathology images. *PLoS ONE* **15**, e0233678 (2020).
25. W. Bulten, *et al.*, Automated deep-learning system for Gleason grading of prostate cancer using biopsies: a diagnostic study. *Lancet Oncol.* **21**, 233–241 (2020).
26. A. Cruz-Roa, *et al.*, Accurate and reproducible invasive breast cancer detection in whole-slide images: A Deep Learning approach for quantifying tumor extent. *Sci. Rep.* **7**, 46450 (2017).
27. S. Nath, G. R. Devi, Three-dimensional culture systems in cancer research: Focus on tumor spheroid model. *Pharmacol. Ther.* **163**, 94–108 (2016).
28. F. Pampaloni, B.-J. Chang, E. H. K. Stelzer, Light sheet-based fluorescence microscopy (LSFM) for the quantitative imaging of cells and tissues. *Cell Tissue Res.* **360**, 129–141 (2015).
29. Z. Wang, *et al.*, Spatial light interference microscopy (SLIM). *Opt. Express* **19**, 1016–1026 (2011).
30. Y. Park, C. Depeursinge, G. Popescu, Quantitative phase imaging in biomedicine. *Nat. Photonics* **12**, 578–589 (2018).

31. A. J. Dominijanni, M. Devarasetty, S. D. Forsythe, K. I. Votanopoulos, S. Soker, Cell Viability Assays in Three-Dimensional Hydrogels: A Comparative Study of Accuracy. *Tissue Eng. Part C Methods* **27**, 401–410 (2021).
32. E. R. Spiller, *et al.*, Imaging-Based Machine Learning Analysis of Patient-Derived Tumor Organoid Drug Response. *Front. Oncol.* **11**, 771173 (2021).
33. B. Gantenbein-Ritter, C. M. Sprecher, S. Chan, S. Illien-Jünger, S. Grad, Confocal imaging protocols for live/dead staining in three-dimensional carriers. *Methods Mol. Biol.* **740**, 127–140 (2011).
34. R. T. Powell, *et al.*, deepOrganoid: A brightfield cell viability model for screening matrix-embedded organoids. *SLAS Discov.* **27**, 175–184 (2022).
35. R. de Hoogt, *et al.*, Protocols and characterization data for 2D, 3D, and slice-based tumor models from the PREDECt project. *Sci. Data* **4**, 170170 (2017).
36. M. Barbier, *et al.*, Ellipsoid Segmentation Model for Analyzing Light-Attenuated 3D Confocal Image Stacks of Fluorescent Multi-Cellular Spheroids. *PLoS ONE* **11**, e0156942 (2016).
37. Z. Chen, *et al.*, Automated evaluation of tumor spheroid behavior in 3D culture using deep learning-based recognition. *Biomaterials* **272**, 120770 (2021).
38. O. Sirenko, *et al.*, High-content assays for characterizing the viability and morphology of 3D cancer spheroid cultures. *Assay Drug Dev. Technol.* **13**, 402–414 (2015).
39. M. Kijanska, J. Kelm, “In vitro 3D Spheroids and Microtissues: ATP-based Cell Viability and Toxicity Assays” in *Assay Guidance Manual*, G. S. Sittampalam, *et al.*, Eds. (Eli Lilly & Company and the National Center for Advancing Translational Sciences, 2004).
40. C. R. Archer, *et al.*, Characterization and validation of a human 3D cardiac microtissue for the assessment of changes in cardiac pathology. *Sci. Rep.* **8**, 10160 (2018).
41. P. Choudhry, High-Throughput Method for Automated Colony and Cell Counting by Digital Image Analysis Based on Edge Detection. *PLoS ONE* **11**, e0148469 (2016).
42. D. Lacalle, *et al.*, SpheroidJ: An Open-Source Set of Tools for Spheroid Segmentation. *Comput. Methods Programs Biomed.* **200**, 105837 (2021).
43. X. Bian, *et al.*, A deep learning model for detection and tracking in high-throughput images of organoid. *Comput. Biol. Med.* **134**, 104490 (2021).
44. J. Chalfoun, *et al.*, MIST: Accurate and Scalable Microscopy Image Stitching Tool with Stage Modeling and Error Minimization. *Sci. Rep.* **7**, 4988 (2017).
45. J. L. Muhlich, *et al.*, Stitching and registering highly multiplexed whole-slide images of tissues and tumors using ASHLAR. *Bioinformatics* **38**, 4613–4621 (2022).
46. J. R. A. Balak, J. Juksar, F. Carlotti, A. Lo Nigro, E. J. P. de Koning, Organoids from the Human Fetal and Adult Pancreas. *Curr. Diab. Rep.* **19**, 160 (2019).
47. L. Abdul, *et al.*, D-CryptO: deep learning-based analysis of colon organoid morphology from brightfield images. *Lab Chip* **22**, 4118–4128 (2022).
48. J. M. Matthews, *et al.*, OrganoidD: A versatile deep learning platform for tracking and analysis of single-organoid dynamics. *PLoS Comput. Biol.* **18**, e1010584 (2022).
49. K. He, G. Gkioxari, P. Dollar, R. Girshick, Mask R-CNN in *IEEE International Conference on Computer Vision (ICCV)*, (IEEE, 2017), pp. 2980–2988.

50. S. J. Pan, Q. Yang, A survey on transfer learning. *IEEE Trans. Knowl. Data Eng.* **22**, 1345–1359 (2010).
51. Y. Rubner, C. Tomasi, L. J. Guibas, The Earth Mover's Distance as a Metric for Image Retrieval. *International Journal of Computer Vision* **40**, 99–121 (2000).
52. J. Wang, *et al.*, The Effect of Magnetic Poly(lactic-co-glycolic acid) Microsphere-Gelatin Hydrogel on the Growth of Pre-Osteoblasts Under Static Magnetic Field. *J. Biomed. Nanotechnol.* **16**, 1658–1666 (2020).
53. E. V. Sazonova, M. S. Chesnokov, B. Zhivotovsky, G. S. Kopeina, Drug toxicity assessment: cell proliferation versus cell death. *Cell Death Discov.* **8**, 417 (2022).
54. W. Xiao, *et al.*, Matrix stiffness mediates pancreatic cancer chemoresistance through induction of exosome hypersecretion in a cancer associated fibroblasts-tumor organoid biomimetic model. *Matrix Biology Plus* **14**, 100111 (2022).

Figures and Tables

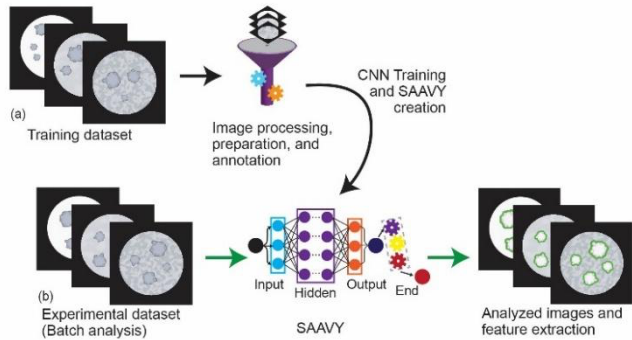


Figure 1. Overview of the SAAVY Training and Validation approach. A) The training method for SAAVY is identified where we processed the images for annotation and user-supervised training. During this training step is where we developed the viability algorithm based on expert-determined characteristics for generating viability estimates. The training data set was 30 images and required approximately 1 hour. B) Batch analysis was run on the experimental (validation) data set images were passed through SAAVY, which identified the mask of the region of interest in green and output a .csv file with other measured information about the image. Analysis time per image was ~ 0.3 seconds. Both training time and analysis time are dependent on the computational power available and could be further accelerated.

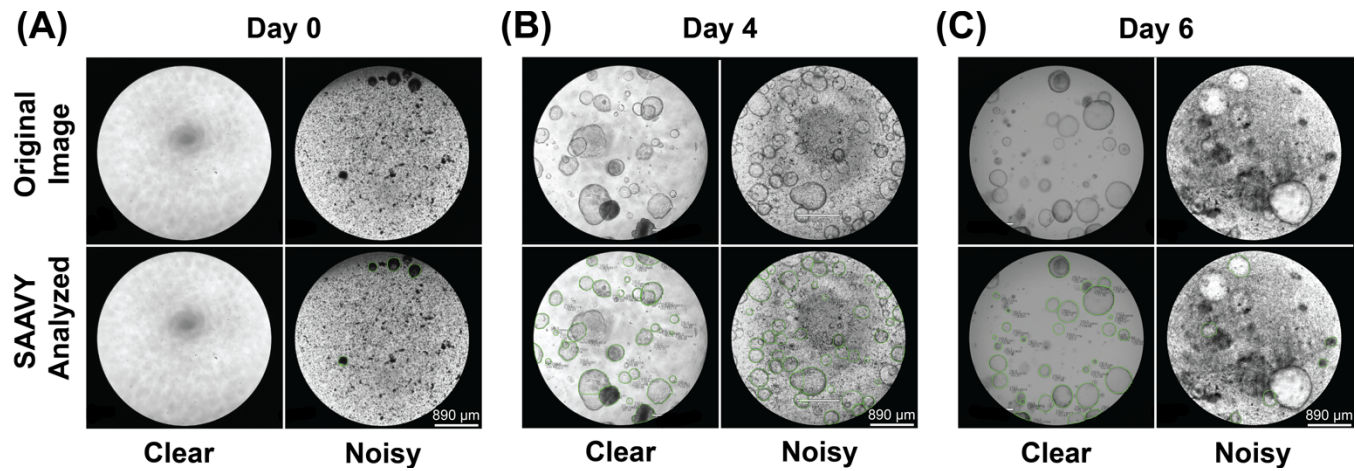


Figure 2. Images representative of before (top row) and after (bottom row) SAAVY analysis. The images are further subset by day: a) D0, b) D4, c) D6). For each day, both clear (no added nanoparticles) and noisy (5 mg/mL of added nanoparticles) images are shown. These are representative images selected from the total 416 images analyzed. Scale bar is 890 μm .

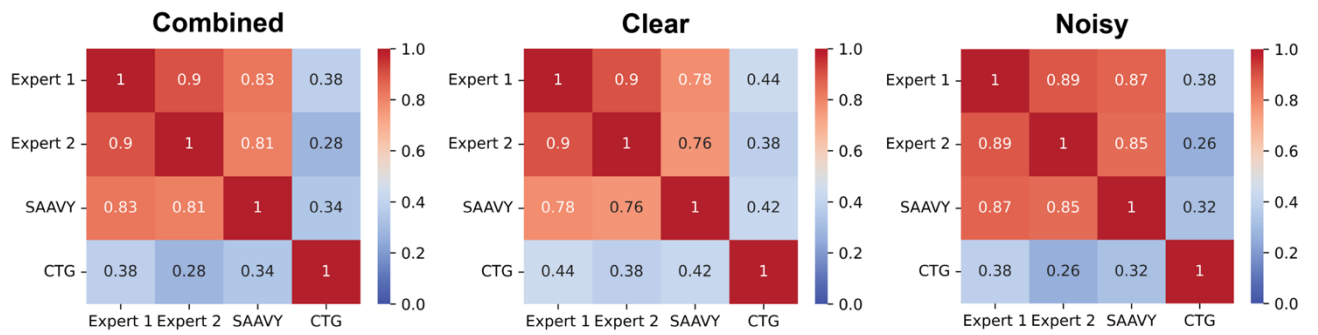


Figure 3. Pearson's R correlation analysis presented as heatmaps comparing Experts, SAAVY, and CTG for the Overall (Combined), Clear background, and Noisy background datasets. Red indicates R values closer to 1 (perfect, positive correlation) and blue indicates no correlation. CTG values are poorly correlated to all other measurements regardless of the data subset. This is likely due to the relative interpretability of CTG results.

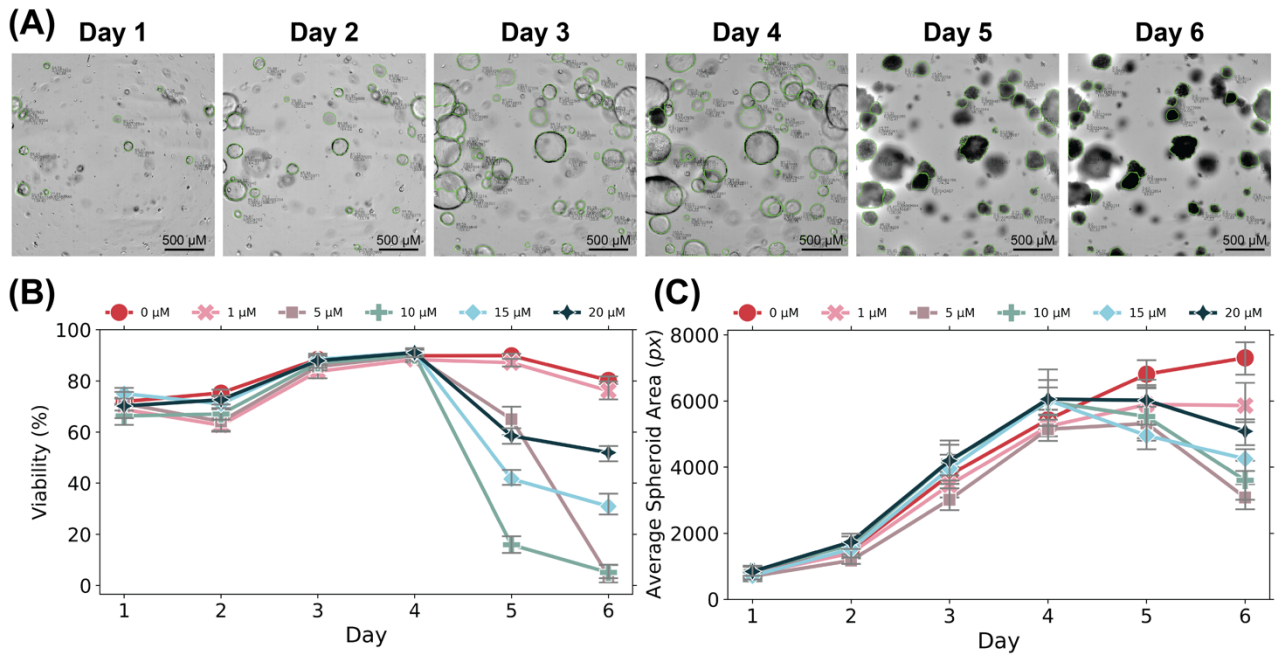


Figure 4. Longitudinal analysis of PDAC response to gemcitabine. A) Images on the top row depict a representative sample well during each day of a six-day dose-response assay. The chosen well was treated with 10 μ M drug (gemcitabine) on Day 4 after imaging. Images are of the same focal plane (320 μ m) throughout the course of the experiment. The scale bar is 500 μ m. B)/C) Line plots of SAAVY application to analyze the viability and growth of spheroids across the dose-response experiment where: B) The raw viability of each drug-response group over the assay and C) the average spheroid area (px) of each drug-response group over time.

Table 1. Summary of calculated metrics comparing Expert 1, Expert 2, and SAAVY throughout each sample sub-grouping (day and background type). Spheroid identification (ID) and live/dead (LD) analysis across all days and background types are presented first. Dashes (-) are noted in columns where that method was used as either the ground truth (Expert 1) or standard for comparison (SAAVY). Similarity and reliability are then quantified for each distribution comparison. We used the Earth Mover's distance to quantify the similarity between the two distributions and Krippendorff's alpha to quantify the reliability of each expert. Equations for accuracy and F1-score calculations are included in the Supplemental. Red cell highlights indicate better performance whereas blue values indicate weak performance.

Day 0						
	Clear			Noisy		
	Expert 1	Expert 2	SAAVY	Expert 1	Expert 2	SAAVY
	98.60%	0%	47.10%	98.60%	50%	32.90%
ID Accuracy	0.093	0.086	-	0.119	0.073	-
Similarity	-0.066	-0.157	-	-0.192	-0.154	-
Reliability						
Day 4						
	Clear			Noisy		
	Expert 1	Expert 2	SAAVY	Expert 1	Expert 2	SAAVY
ID F1-Score	-	1	1	-	0.992	0.992
LD F1-Score	-	1	1	-	0.992	0.992
Similarity	0.029	0.073	-	0.021	0.036	-
Reliability	0.531	-0.202	-	0.869	0.735	-
Day 6						
	Clear			Noisy		
	Expert 1	Expert 2	SAAVY	Expert 1	Expert 2	SAAVY
ID F1-Score	-	1	1	-	0.984	0.992
LD F1-Score	-	0.914	0.891	-	0.962	0.954
Similarity	0.045	0.048	-	0.016	0.011	-
Reliability	0.869	0.861	-	0.863	0.854	-

Supporting Information for

Nondestructive, quantitative viability analysis of 3D tissue cultures
using machine learning image segmentation

Kylie J Trettner^{1,2}, Jeremy Hsieh³, Weikun Xiao², Jerry SH Lee^{1,2,4}, Andrea M. Armani^{1*}

Andrea M. Armani

Email: aarmani@eit.org

This PDF file includes:

Supporting text

Figures S1 to S8

Tables S1 to S3

Legends for Datasets S1 to S5

SI References

Other supporting materials for this manuscript include the following:

Datasets S1 to S5

Software S1

Supporting Information Text

3D Culture Preparation

Nanoparticle Synthesis. We synthesized iron oxide (Fe_3O_4) nanoparticles using a previously reported air-free, coprecipitation method summarized here. First, we purged 20 mL of DI water in a three-neck round bottom flask with nitrogen while we measured 1 g of iron (II) chloride and 0.4 g of iron (III) chloride in an argon glovebox. We transferred the iron chloride reactants and added them to the reaction flask using a solids addition flask. We then stirred the reaction solution using a stir bar, submersed the reaction flask in a mineral oil bath, and heated it until the reaction solution reached 80 °C. Once this temperature point was reached, 5 mL of ammonia hydroxide was added dropwise to the reaction flask. We increased the stirring speed during this step to avoid possible morphological changes to the nanoparticles caused by the magnetic stir bar. The reaction refluxed for one hour before the flask was removed from heat and allowed to cool. Once cool, we collected the magnetic particles into a falcon tube and centrifuged the collected material. After centrifugation, we decanted the water and then resuspended the particles in DI water to wash. We repeated the centrifugation and wash steps 3x before massing the final solutions to determine the yield and concentration of nanoparticle solutions. Using the nanoparticles, a series of solutions were prepared. The final concentrations of nanoparticles in the studied seeded wells were: 0.5, 1, 1.5, 2, 2.5, 3, 5, and 10 mg/mL.

Hydrogel Preparation. Two hydrogel materials were used during this study: 1) Matrigel (Corning) and 2) Basement Membrane Extract or BME (Cultrex). The specific Matrigel used was growth factor reduced, phenol red-free (Cat. No. 356231) of one of two lots (0258005 or 0322001). The BME used was reduced growth factor (Cat. No. BME001-05) of one of two lots (1617263 or 1661425). Matrigel and BME are prepared by first thawing the initial bottle (either 5 or 10 mL) on ice overnight in a 4°C cold room. Once thawed, 1 mL aliquots were made with extra precaution not to create any bubbles when transferring. Aliquots were placed in -20°C (Matrigel) or -80°C (BME) freezer until use. When preparing for cell seeding, aliquots were placed on ice at room temperature in the tissue culture hood (biosafety cabinet) for up to an hour until thawed. We placed the 96-well plates in an incubator to warm up while the gel was thawing.

Once thawed, the hydrogel liquid is ready for use. We removed gel from the cell-laden or mixed nanoparticle-gel solutions in 10 μL increments and plated it in the middle of the well. We used 4-6 replicates of each condition to average out potential experimental variabilities. Once the plate was seeded with gels, we flip them and place them in an incubator to warm up and induce thermal sol-gel transition of the material for 15 minutes. Once complete, we removed the plates, added 100 μL of media into each well, placed 100 μL of PBS in surrounding, emptied wells as an evaporation buffer, then returned the plates to the incubator until performing the imaging study.

Cell Media. We used two different media, mouse splitting media (MSM) and the Complete Feeding Media (CFM), to culture PDAC spheroids as previously published (1). MSM was made by combining then filtering 485 mL of advanced DMEM/F12, 5 mL of Pen/Strep, 5 mL of GlutaMax, and 5 mL of HEPES. MSM served as a base for CMF, which we made in 200 mL batches. We used 173 mL of MSM and supplemented the media with 20 μL each of A-83-01, mEFG, hFGF-10, and hGastin I. Further supplementation included 200 μL of mNoggin, 500 μL of N-acetylcysteine, 2 mL of nicotinamide, 20 mL of R-Spo1 conditioned media, and 4 mL of B27.

Cell-laden Hydrogel Solutions. To prepare cell-laden hydrogel solutions, we first removed media using an aspirating pipette from wells containing previously cultured spheroids. The number of wells was pre-determined by how many wells must be seeded for the experiment. We then washed each well with 500 μL of Dulbecco's phosphate buffered saline (PBS) by running it down the side of the well to not disturb the hydrogel dome. We let PBS sit for up to 2 minutes before aspirating. Then we added 500 μL of

Gentle Cell Dissociate Buffer to each well and scraped the wells using a 1000 μ L pipette tip.

We collected all dissociated hydrogel and cell material from each well in a 15 mL conical tube. The tube was placed on a rocker in the 4 °C cold room for 1 hour. Then, we mixed the solution using a p1000 pipette by manually resuspending the cell, hydrogel, and dissociation buffer solution 20 times. We spun down this solution at 300 rcf for 5 minutes. Once centrifuged, we aspirated the supernatant and added 1 mL of fragmenting solution (500 μ L TrypLE, 500 μ L PBS, 1 μ L DNase I) and gently agitated the solution for 5 minutes at room temperature. We quenched the trypsin reaction by adding three times the volume in the conical tube (3 mL) of cell media, mixed the solution, and then centrifuged the solution for another 5 minutes at 300 rcf. We then aspirated the solution above the cell pellet and resuspended it with 500 μ L of cell media before straining the resuspended cells through a sterile 70 μ m filter. We washed the initial tube with 500 μ L media and strained it before counting the cells using a BioRad TC10 automated cell counter. We calculated the number of cells needed for the experiment and removed the appropriate aliquot from the cell solution before centrifuging for 5 minutes at 300 rcf. We aspirated the media and resuspended the cell pellet in the calculated amount of thawed hydrogel for direct plating or further use in nanoparticle gels.

Nanoparticle Hydrogel Solutions. When mixing solutions with nanoparticles, we first calculated the volume of nanoparticles needed from the stock solution to create a desired gel concentration at a specific volume. The volume is typically determined by the number of wells (10 μ L of gel solution per well). For example, if our stock solution is 54 mg/mL, preparing 150 μ L of gel (12 wells plus some extra) requires 2.78 μ L of stock to obtain a final concentration of 1 mg/mL. We place the stock solution aliquot in a 1.5mL centrifuge tube and spin in a benchtop centrifuge for up to 5 minutes until the nanoparticles are separated from the initial solution. Then, we will remove the excess water using a micropipette, add the cell-laden hydrogel solution to the nanoparticles, and manually resuspend the particles. Extra care is taken not to introduce bubbles into the gel and to distribute the cells and nanoparticles evenly in the solution before plating in 10 μ L increments in the middle of the desired well.

Dataset Generation

The spheroid samples were analyzed using 1) imaging and 2) human expert evaluation. Imaging was performed throughout the experiment. Expert evaluation was formally completed on images chosen for this study. A subset of data was also analyzed using CellTiter Glo (CTG) assay.

Imaging. Images of PDAC samples were taken for the study on an ECHO Revolve using an Olympus 4x lens on the day of seeding (D0), the day of chemotherapeutic treatment when applicable (D4), and on day 6 (D6) before developing the CTG assay. Spheroids were incubated the entire time and were only removed from the incubators for imaging or treatment.

For the longevity study, images were taken on an Operetta CLS with a 5x lens on all days of the assay (D0-D6). This instrument features an incubator chamber, and cells were maintained at 37 °C and 5% CO₂ except for when they were transferred from the incubator to the instrument.

Human Evaluation. Experts were chosen according to their training on 3D tissue culture protocols, viewing or imaging spheroids with microscopes, and familiarity with cystic spheroid systems. We asked the experts to take all spheroids in the image into account. If images appeared to have no spheroid structures experts were asked to note this; otherwise, they provided their estimation of aggregate spheroid viability for the entire image. Experts were asked to time themselves during estimation to provide basis for efficiency comparison as well.

Images analyzed in the main text were randomly selected for inclusion. Images were renamed with the image number index according to the order in which they were selected to blind them before providing images for expert analysis. We further discuss expert variability and establishment of ground truth in subsequent sections Establishing ground truth and Incremental estimation of human analysis compared to SAAVY.

CellTiter Glo. CellTiter Glo (CTG) is a luminescence-based viability assay commercialized by Promega. We use the procedure provided by Promega to conduct our analysis. Briefly, CTG reagent is removed from storage freezers to thaw overnight at 4 °C before use in the assay. Well plates are removed from the incubator and the reagent is removed from the fridge to equilibrate to room temperature 30 minutes before development. In 96-well format, 100 µL of CTG reagent is added into each well for development. The well plates are placed on a shaker for 5 minutes before 20 minutes of wait time for the reagent to react with lysed cellular material. The plates are then read on a BioTek plate reader, and the results are exported in Excel format for normalization.

The normalization process includes subtracting the average material background from control wells which are typically hydrogel matrix and cell media from the experiment wells. Cell control wells are used as the positive control for completely alive cells. The average luminescent signal of cell control wells is used as the divisor for all experiment wells. All final reported CTG values are normalized in this manner.

SAAVY Development

An overview of the key elements of SAAVY is shown in Figure SI-1. Notably, all programming is performed in Python. PyTorch was chosen as our backend framework because of its speed and simplicity. The conda environment file is available within GitHub; however, instructions for installation differ slightly based upon the availability of a CUDA capable GPU. SAAVY was trained and tested on an Nvidia RTX 3080 with 12 GB of VRAM, Intel Core i9 10850K CPU. The images are rescaled during inference to fit into most GPUs with less than 4GB of VRAM.

SAAVY Design. SAAVY is composed of two high level steps: spheroid segmentation and individual spheroid analysis. The segmentation step is a Mask R-CNN PyTorch model, which adds the ability to mask segmented instances for individual analysis of spheroids. Mask-RCNN is highly performant in instance segmentation and is based off Faster R-CNN (2) which predicts bounding boxes, and class scores for potential objects in an image. We elected to start from the MS COCO pretrained dataset to implement transfer learning and refined the model from there. The box predictor and mask predictor were both replaced and trained on our dataset. We ran our analysis on each of the masked spheroids as outlined in Figure SI-1.

Training Dataset Creation. The training dataset was comprised of 24 images balanced between day (Day 4 and Day 6), status (alive and dead), and background type (clear and noisy), as noted in Table SI-1. Per the protocol, the data was resized to 1290 x 1210 (px). Then, the experts annotated each spheroid inside the image using VIA Image Annotator (2.0.11, Oxford). A class label was manually assigned to each spheroid where the “cell” class label is used for all detections. The saved annotations were exported in the COCO file format.

Model Training. Using supervised learning, SAAVY was trained using the annotated images for 20 epochs saving checkpoints and Tensorboard updates at the end of each cycle. The images should be scaled accordingly to fit into VRAM. Images with dimensions of 1200x900 fit into most 4 GB GPUs. Learning rate and similar training parameters were based on those used by Matterport’s M-RCNN examples. Based on the validation loss and epoch loss, we used the checkpoint at epoch 15 when improvement stops (Figure SI-2).

Prediction and Analysis. As part of the algorithm, we developed an equation that compares the average intensity of the masked regions of interest against the overall background intensity of an image. Further, we included a distance penalty that relates the pixel of interest to the overall background intensity and a minimum tolerance that serves as the minimum boundary condition on the intensity for appropriate viability assessment. Both values were determined by expert analysis and comparison during the initial setup. A lower distance penalty results in a smaller viability decrease per unit of intensity decrease, and the minimum tolerance allows for spheroids without complete transmittance to be classified as 100% alive. To determine the minimum tolerance, we noted the intensity of a 100% alive spheroid, as determined by expert analysis, and compared it to the background intensity of an image without nanoparticles.

The trained weights checkpoint was loaded using Pytorch, and we use that to inference each image. The output is a list of tagged spheroids and vertices of their masks. This information is passed to the next step, which creates a mask using the vertices and inverts it to calculate the mean background intensity. Then, it iterates through each set of vertices to calculate the mean spheroid intensity. The eccentricity of each spheroid and its size are also determined at this step. The final viability of an individual spheroid is calculated by comparing the ratio of the spheroid intensity against the background intensity, as noted in EQ-1.

$$\text{EQ-1} | \text{Viability} = 1 - \frac{\text{clamp}(\text{Background} - \text{Minimum Tolerance} - \text{Mean Value})}{\text{Distance Penalty}}$$

Based on this expression, a healthy spheroid is mostly translucent whereas a dead spheroid is entirely opaque. This process was completed for each spheroid. The viability of the entire well is determined by averaging individual spheroid viability across the entire image. Finally, the vertices are drawn and connected to the original images with individual spheroid information.

Analysis

Relevant Equations for the Confusion Matrix. Equations 2 and 3 were calculated from the confusion matrix to characterize the performance of SAAVY at identifying spheroid/no spheroid and live/dead spheroids throughout the analysis.

$$\text{EQ-2} | \text{Accuracy} = \frac{\text{true positives (TP)} + \text{true negatives (TN)}}{\text{actual positives (P)} + \text{actual negatives (N)}}$$

$$\text{EQ-3} | \text{F1 score} = 2 * \frac{\text{precision} * \text{recall}}{\text{precision} + \text{recall}}$$

Exploratory Comparison Analysis. Pearson's correlation was used to compare SAAVY to Experts and CTG and is plotted as heatmaps in Figure SI-3. CTG comparisons are only included where appropriate, as we only have matched samples on Day 6. For the Day 0 and Day 4 data sets, CTG was not included on the correlation matrices for clarity of the plot.

Distance Metrics. We compared Jensen Shannon Distance (JSD), Kullback Leibler Divergence (KL), Earth Mover's Distance (EMD), and Population Stability Index as distance metrics. JSD, KL, and EMD values depend strongly on the bin width chosen, as the data was discretized in a histogram before use. We calculated the ideal number of bins using the Freedman-Diaconis rule (EQ-4) to find the bin width and then divided the range of values in the data set by the bin width. These were calculated as follows: 4 for Expert 1, 8 for Expert 2, and 8 for SAAVY. Since this binning strategy would significantly compress the overall data, we proceeded with a distribution that binned our data in 10% viability increments. Due to the output of "none detected" that we coded as "-1", we used 11 total bins from -10 to 100 (inclusive).

$$\text{EQ-4} | \text{Bins} = \text{ceil} \left(\frac{\text{data range}}{\text{bin width}} \right); \text{bin width} = 2 \left(\frac{\text{inter-quartile range}}{\sqrt[3]{n}} \right)$$

We also included Krippendorff's alpha, a reliability metric, to evaluate systemic differences between methods of viability estimation for the experts and SAAVY comparisons. The results of these comparisons are included in Table SI-2.

Establishing Ground Truth. AI segmentation algorithms depend on ground truth data for appropriate model training and once trained, should be compared to ground truth to evaluate the overall model performance. One strategy is to have experts serve as ground truth. Therefore, before assessing SAAVY's overall performance, the images were analyzed by a pair of experts, and the results were compared to confirm consistency.

Typically, when an expert evaluates brightfield images of spheroids for viability, they consider several factors, including their morphology and opacity. For example, a more opaque (or darker) spheroid is less viable. In this context, the ability of an expert to correctly identify grayscale values repeatedly is one strategy to test their reliability. An important note here is that we considered the ground truth of all D0 images to be "no spheroid" because not enough time has passed for the single-cell fragments to self-assemble into a spheroid structure. Thus, the ground truth discussion only refers to images from D4 and D6. If no spheroids were detected in the image, the viability is labeled as "none detected."

As part of the effort to establish ground truth, we wrote a program that would randomly pick a shade of gray and asked the experts to predict the percent white of the image (i.e., a 0% white image is black, and a 100% white image is white). The code recorded and output the expert-estimated value and the true percent value of the shade. Using the same distribution visualization and JSD calculations detailed in the main text, we found that Expert 1 more accurately assessed the true intensity value in an image (Figure SI-4).

Expert 1 has a lower Jensen Shannon distance (0.140577) than Expert 2 (0.386908), suggesting that the distribution of Expert 1 is closer to that of the truth, although both are considered significantly different distributions than the respective truth. Expert 2 displayed gaps in prediction between 60% to 80%, thus missing a large portion of grey value differences, whereas Expert 1 estimated within the entire range of binned valued. Therefore, we decided to move forward with Expert 1 as our ground truth for the classification of SAAVY.

The experts' analyses follow a similar trend when looking at the data analyzed in the main text. In comparison with Expert 2, Expert 1 more frequently predicts viability ranges between 25% to 75%, which aligns with the statistical nature of biological systems growth. Further, the resolution of the viability assignments is very coarse and dependent on the expert. Expert 1 assigns in 5% increments, and Expert 2 uses 10% increments. This binning of the data reduces the accuracy of viability assessment.

To explore the role of background noise in expert analysis, the data is subset into clear and noisy backgrounds. Once this division is made, it becomes apparent where the experts diverged in their analysis. When the background is clear, Expert 2 assigns fewer samples to viabilities between 20-70% and missed regions of estimation as compared to Expert 1. Given the apparent bias in Expert 2's analysis, Expert 1 was used as the ground truth in subsequent comparisons.

Incremental estimation of human analysis compared to SAAVY. In figure SI-6, we display the data distributions for all spheroids estimated at ≥ 0 in 100 bins to provide the count of estimated viability in 1% incremented bins. During our analysis, we noticed that human estimation is biased in similar ways to the grayscale analysis in Figure SI-4. The experts showed patterns in how they assigned values and assigned them in roughly 5% (for Expert 1) and 10% (for Expert 2) ranges. SAAVY clearly displays a distribution of viabilities across the entire range with minor gaps in increments that are more likely attributed to not having an image fall within the specified range.

Visualizing the Data Distributions. In Figure SI-7, we plot the distributions of the Expert to SAAVY comparisons from the main section of the manuscript. The distributions from Day 0 (A and B) reflect the poor reliability between Experts and SAAVY due to the handful of times that SAAVY records a viability on part of the image even though no spheroid is present according to

ground truth. This reliability, however, improves on Day 4 and Day 6 as we note the convergence of the distributions between both experts and SAAVY.

The breakdown of CTG data as compared to SAAVY in combined, clear and noisy background subsets is presented in Figure SI-8. In direct comparison, CTG values over 100% do not seem intuitive. However, it is important to state that these values are relative to the plate, and they make sense within the specific assay the results belong to. Note that CTG cannot produce values of 0 or below, and SAAVY only reports 0-100%.

Other Statistical Analyses. The Shapiro test was used to determine normality of all data before statistical hypothesis testing. Where data was significantly large for all groups being studied, the central limit theorem approximation of normality was used. All data is paired, so related t-test and repeated measures ANOVA with Tukey HSD post-hoc analyses were used for large data with two groups or more than two groups for comparison, respectively. For paired (dependent), nonparametric data, Wilcoxon signed-rank test was used, and we ensured the data did not include a large proportion of matched values.

All analyses were implemented in Python using `scipy`, `scipy.stats`, `pingouin`, `sklearn`, `math` libraries, and the associated functions for the above calculations. The population stability index function came from a GitHub reposition [\(3\)](#).

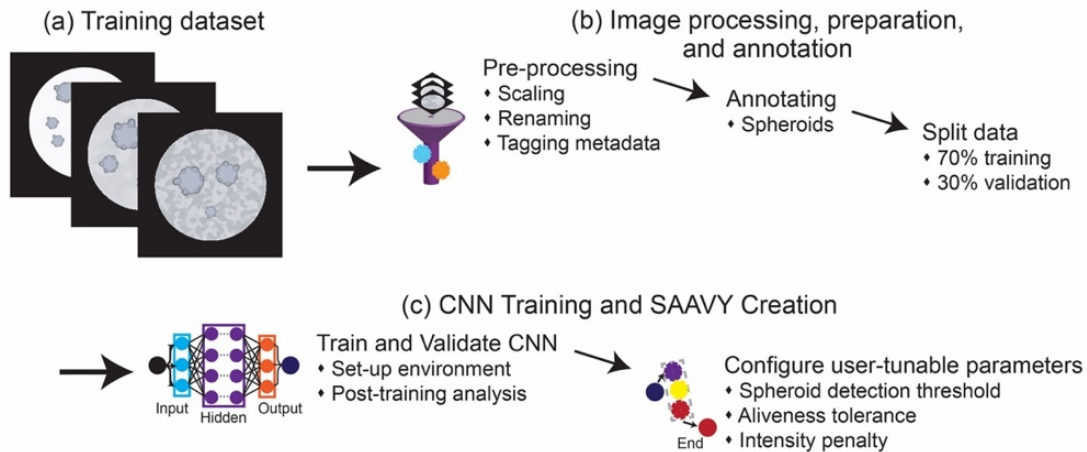


Fig. S1. Overview of SAAVY training process. a) 30 images were randomly selected for use as the training data set, b) the image processing step included rescaling the images to workable sizes and annotating 24 (70%) of the randomly selected training images and c) SAAVY validation on the remaining 9 (30%) images of the data set and some fine-tuning of parameters for best performance.

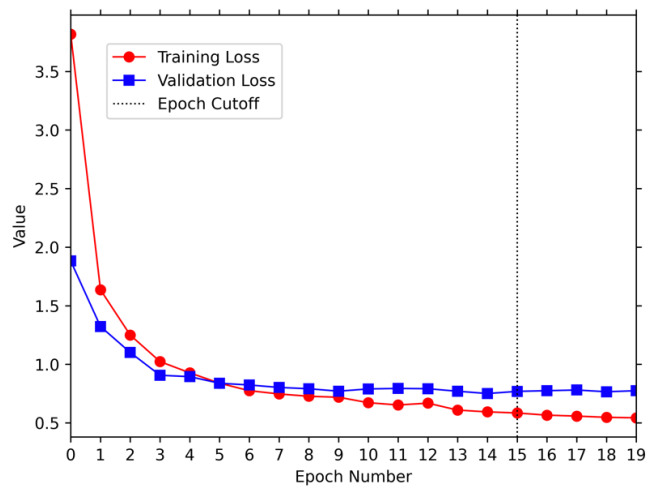


Fig. S2. Loss plot denoting the stabilization of loss around the same asymptote for both training and validation loss with the decided-upon epoch cutoff noted at 15.

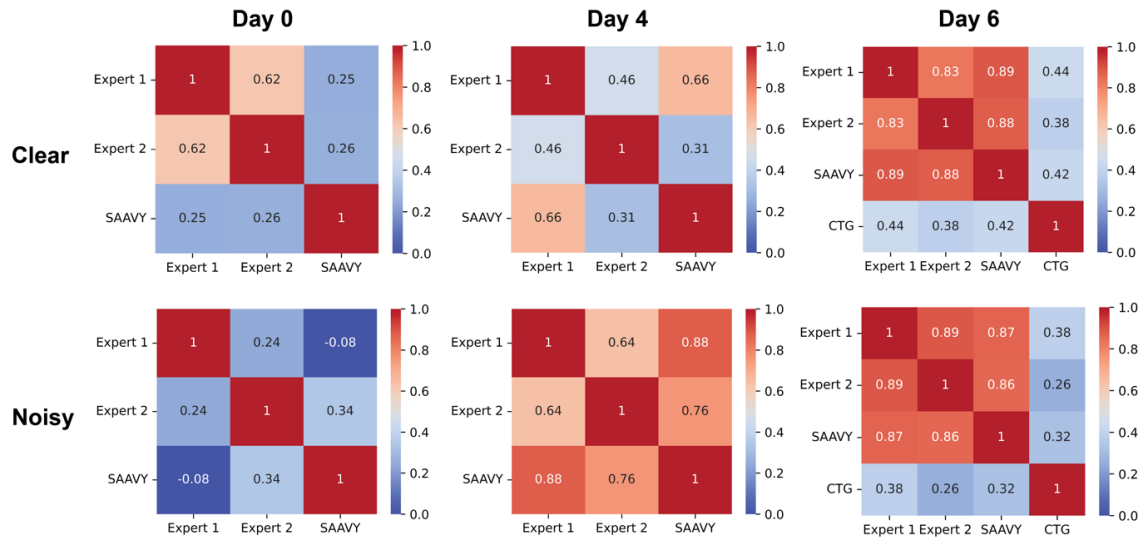


Fig. S3. Heatmap plots of Pearson's correlation between Expert 1, Expert 2, SAAVY and CTG (where appropriate). The plots are subset according to background type with clear backgrounds on the top row and noisy backgrounds on the bottom. Columns representing increases in day (from right to left). Red indicates improved correlation and blue indicates poor correlation.

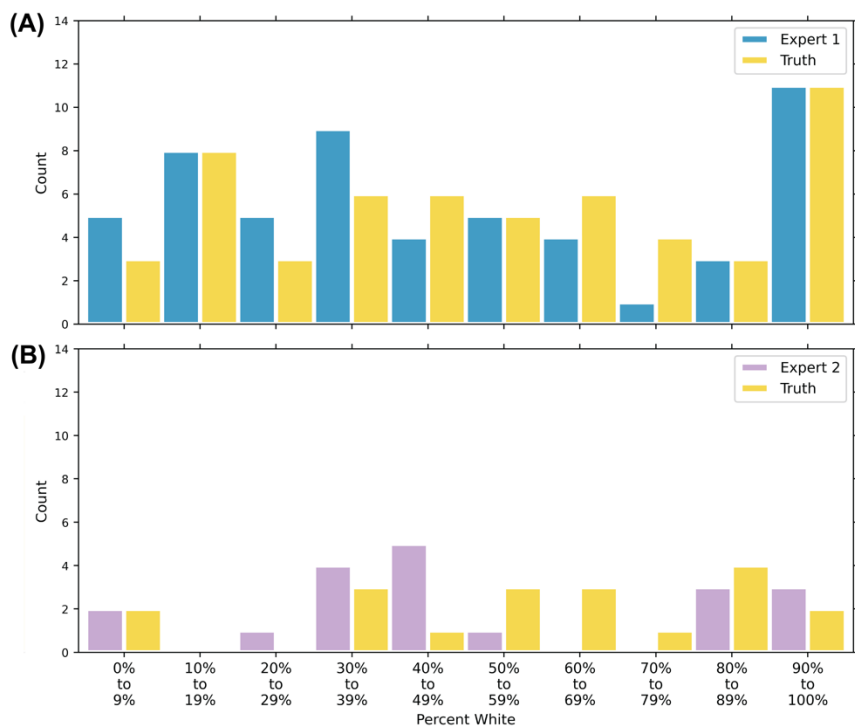


Fig. S4. Analysis of Expert 1 and Expert 2 greyscale assessment compared to ground truth values. a) Expert 1 and b) Expert 2.

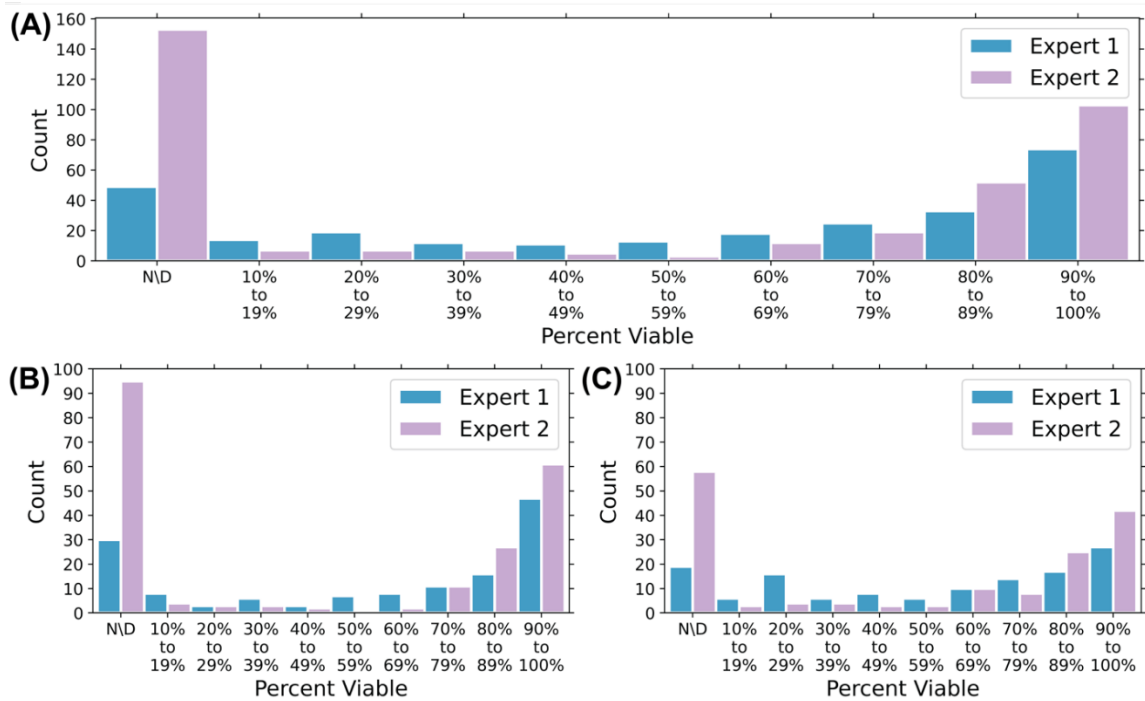


Fig. S5. Expert only histograms of (A) all data, (B) clear background data histogram, and (C) noisy background data histogram. N/D stands for none detected.

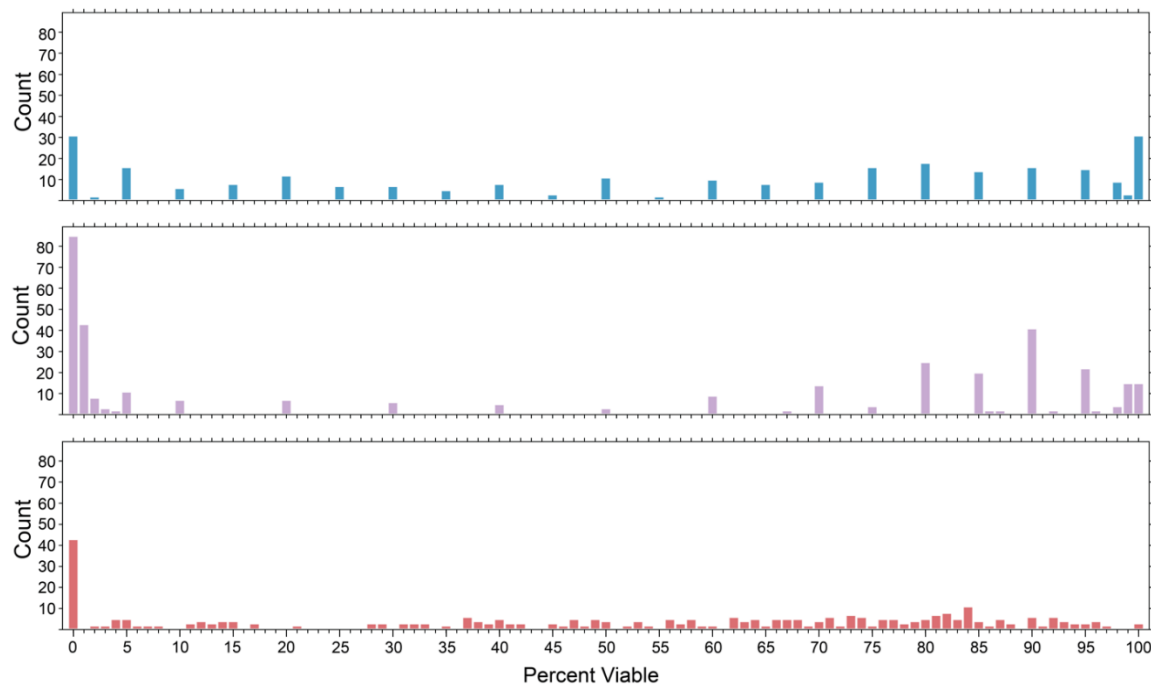


Fig. S6. Individual percent binning of a) Expert 1, b) Expert 2, and c) SAAVY analysis for the same set of images. Expert 1 shows ~5% gaps in estimation, Expert 2 displays ~10% gaps in estimation when far from the extreme edges of the distribution, and SAAVY displays a nearly even distribution without significant gaps in percent viability.

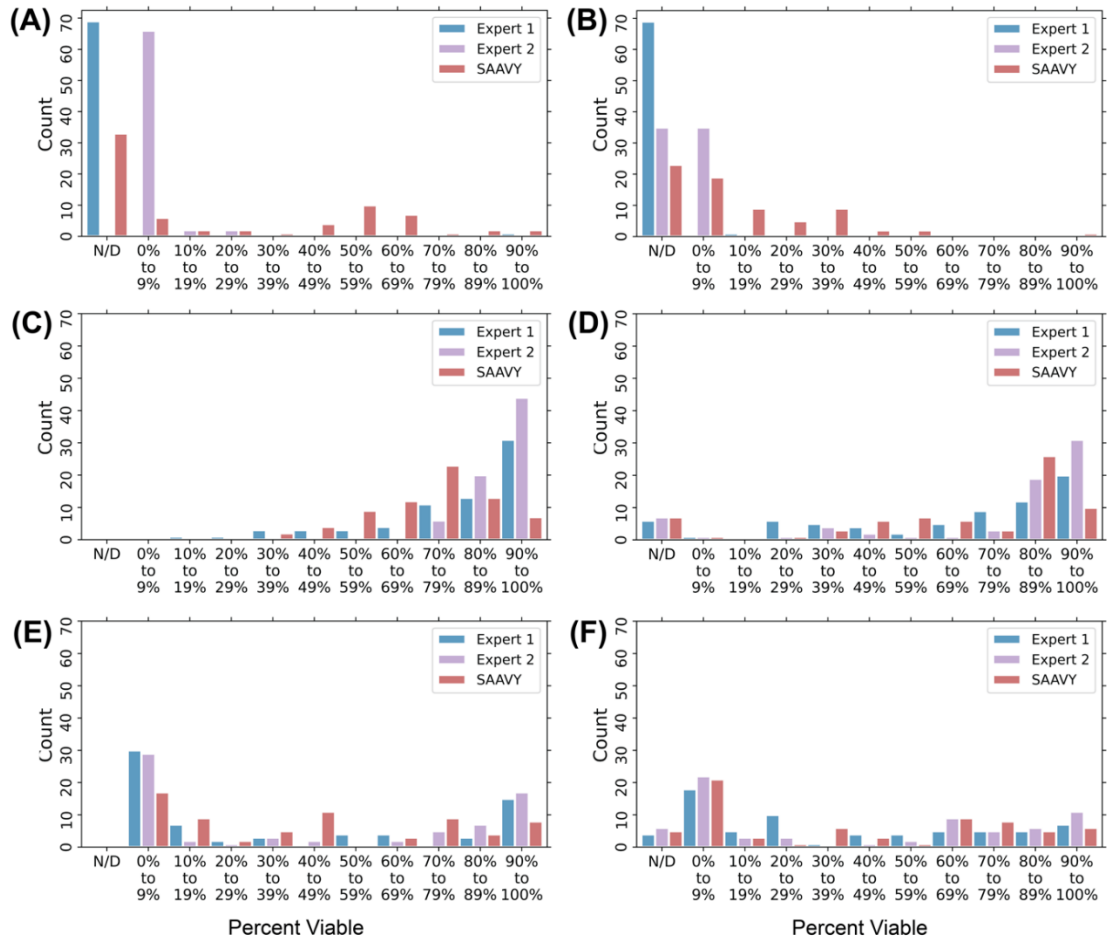


Fig. S7. Histogram distributions of a) Clear Backgrounds comparing Experts 1 and 2 and SAAVY on D0, b) Noisy Background viabilities predicted by Expert 1 and 2 and SAAVY on D0, c) Clear Backgrounds comparing Experts 1 and 2 and SAAVY on D4, d) Noisy Background viabilities predicted by Expert 1 and 2 and SAAVY on D4, e) Clear Backgrounds comparing Experts 1 and 2 and SAAVY on D6, f) Noisy Background viabilities predicted by Expert 1 and 2 and SAAVY on D6. N/D denotes “none detected”. Note that in these images the plot is set to 10% bin increments for ease of view, actual resolution is much finer.

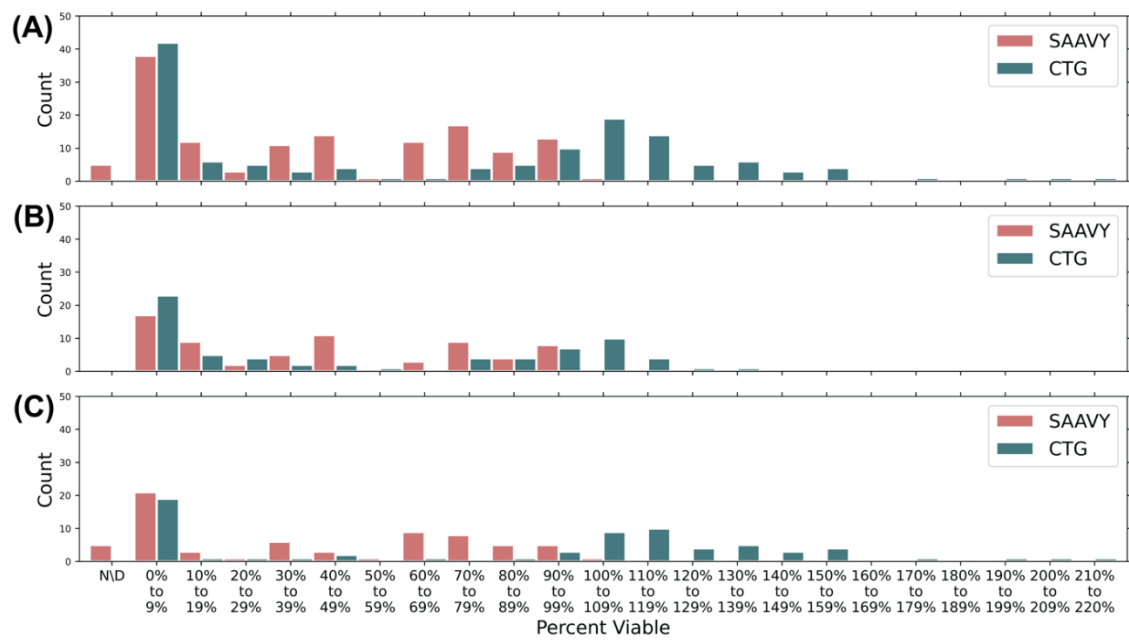


Figure S8. Histogram plots comparing SAAVY and CTG performance across all matched samples in a) the combined dataset, b) the clear subset, and c) the noisy subset. Critically, we display the frequent error of CTG to report greater than 100% viability, and when used in samples that have noisy backgrounds when normalized (with included material standards to adjust for background noise, where appropriate).

Table S1. The table notes the distribution of images included in the training dataset. Of the 24 included, they were balanced by day (12 for each) and background type subset (6 for each day's background subset). We further break down the inclusion of sample viabilities (based on rough groupings) to note that we included representative stages of viability within the training for identifying spheroids.

Day 4		Day 6	
Total	12	Total	12
Clear	6	Clear	6
Dead	0	Dead	0
Mostly Dead	0	Mostly Dead	2
Mostly Alive	3	Mostly Alive	1
Alive	3	Alive	3
Noisy	6	Noisy	6
Dead	1	Dead	3
Mostly Dead	0	Mostly Dead	2
Mostly Alive	3	Mostly Alive	0
Alive	2	Alive	1

Table S2. Summary of all statistics run to compare various distance metrics against each other during exploratory analysis (columns Jensen Shannon – Population Stability Index). All calculations are completed as SAAVY compared to Expert and can be interpreted as Expert distribution being a certain distance from the SAAVY distribution. All metrics except for Kullback Leibler are also mathematically symmetric and can be interpreted as Expert distribution compared to SAAVY. Inf in an abbreviation for infinity, which is achieved when there are 0 data within a given bin of the data distribution. Values closer to 0 indicate distributions that more similar.

		Jensen Shannon	Kullback Leibler	Earth Mover's	Population Stability Index
Day 0	Clear	Expert 1	0.470	0.717	0.094
		Expert 2	0.711	2.261	0.086
	Noisy	Expert 1	0.548	1.052	0.119
		Expert 2	0.406	0.515	0.073
Day 4	Clear	Expert 1	0.334	inf	0.029
		Expert 2	0.533	1.163	0.073
	Noisy	Expert 1	0.266	0.312	0.021
		Expert 2	0.291	0.348	0.036
Day 6	Clear	Expert 1	0.384	inf	0.045
		Expert 2	0.279	0.292	0.048
	Noisy	Expert 1	0.253	0.332	0.016
		Expert 2	0.220	0.163	0.011

Table S3. Image and Experiment Metadata.**Experimental/Sample**

Experimenter Name	KJ Trettner
Experiment Description	imaging and metabolic activity monitoring of PDAC spheroids in the presence of increasing concentrations of nanoparticles
Experiment Date(s)	2021-06-13 through 2021-06-20 , 2021-06-28 through 2021-07-04, 2022-04-27 through 2022-05-03, 2022-05-17 through 2022-05-23, 2023-04-05 through 2023-04-11
Sample Description	pancreatic adenocarcinoma mouse line 8-14F-7: KRAS G12D, PTEN loss, COX2 overexpression, female, 2 weeks old at the time of sacrifice
Medium	Complete feeding medium, made as previously reported (1)
Temperature	37C
CO2	5%

Microscope hardware specifications

Microscope manufacturer(s)	ECHO, Perkin Elmer
Microscope model(s)	ECHO Revolve, Operetta CLS
Objective manufacturer ECHO	Olympus
Magnification/NA ECHO	5x/0.16
Objective manufacturer CLS	OperaPHX/OPRTCLS
Magnification/NA CLS	5x/0.16
Camera ECHO	5 MP CMOS color camera
Camera CLS	4.7Mpx sCMOS camera (2160x2160), 16 bit resolution, 6.5um pixel size

Image acquisition settings

Acquisition date(s) ECHO	2021-06-13, 2021-06-17, 2021-06-19, 2021-06-28, 2021-07-02, 2021-07-04, 2022-04-27, 2022-04-01, 2022-05-03, 2022-05-19, 2022-05-23
Acquisition date(s) CLS	2023-04-05, 2023-04-06, 2023-04-07, 2023-04-08, 2023-04-09, 2023-04-10
Illumination type ECHO	LED

Illumination type	CLS	LED 740nm
Channel name		Brightfield

Dataset S1 (separate file).

Dataset Title: longevity.csv

File = file name of the image analyzed

Count = total number of spheroids identified in the image

avg_viability = the averaged viability of all independently identified spheroid viabilities, measured from 0 to 100

avg_circularity = a measure of how circular the spheroid is, where 1 is perfectly circular, averages from all independently identified spheroids

avg_intensity = the averaged intensity of all independently identified spheroids, measured from 0 to 255 for 8-bit color coding

pct_analyzed = the averaged percent of the image that was included as an identified spheroid region of interest

background_intensity = the averaged intensity of the background that was not included in an identified spheroid region of interest

avg_area = the averaged area of all independently identified spheroids

Dataset S2 (separate file).

Dataset Title: mappings.csv

File = file name of the image analyzed

Count = total number of spheroids identified in the image

avg_viability = the averaged viability of all independently identified spheroid viabilities, measured from 0 to 100

avg_circularity = a measure of how circular the spheroid is, where 1 is perfectly circular, averages from all independently identified spheroids

avg_intensity = the averaged intensity of all independently identified spheroids, measured from 0 to 255 for 8-bit color coding

pct_analyzed = the averaged percent of the image that was included as an identified spheroid region of interest

background_intensity = the averaged intensity of the background that was not included in an identified spheroid region of interest

avg_area = the averaged area of all independently identified spheroids

Dataset S3 (separate file).

Dataset Title: expert_color_match.xlsx

Two sheets: Expert 1 and Expert 2 containing the same information.

Expert 1 (or 2) = the percent white value Expert 1 (or 2) assigned to a randomly generated greyscale image

Truth = the actual percent white value of the randomly generate greyscale image

Dataset S4 (separate file).

Dataset Title: SAAVYTorch-debug_1.1-longevity.xlsx

file = the filename of the analyzed image

count = total number of spheroids identified in the image

avg_viability = the averaged viability of all independently identified spheroid viabilities, measured from 0 to 100

avg_circularity = a measure of how circular the spheroid is, where 1 is perfectly circular, averages from all independently identified spheroids

avg_intensity = the averaged intensity of all independently identified spheroids, measured from 0 to 255 for 8-bit color coding

pct_analyzed = the averaged percent of the image that was included as an identified spheroid region of interest

background_intensity = the averaged intensity of the background that was not included in an identified spheroid region of interest

avg_area = the averaged area of all independently identified spheroids

Day = the day of the experiment (beginning at Day 0 for initial seeding) on which the image was captured

gem_conc = the concentration of gemcitabine, a chemotherapeutic agent, added to the sample well

Dataset S5 (separate file).

Dataset Title: SAAVYTorch-debug_1.1-mappings.xlsx

Sheet1

original_file = the original file name of the analyzed image (these were blinded before SAAVY analysis)

file = the filename that was assigned to the analyzed image during blinding

count = total number of spheroids identified in the image

avg_circularity = a measure of how circular the spheroid is, where 1 is perfectly circular, averages from all independently identified spheroids

avg_intensity = the averaged intensity of all independently identified spheroids, measured from 0 to 255 for 8-bit color coding

pct_analyzed = the averaged percent of the image that was included as an identified spheroid region of interest

background_intensity = the averaged intensity of the background that was not included in an identified spheroid region of interest

avg_area = the averaged area of all independently identified spheroids

Treatment? = yes/no if the image was a well sample that was treated with gemcitabine on Day 4 of the associated experiment

np_c = the concentration of nanoparticles doped into the sample, where appropriate for noisy background study

Day = the day of the experiment (beginning at Day 0 for initial seeding) on which the image was captured

Expert1_viability = the viability (from 0 to 100%) that Expert 1 assigned to the image

Expert2_viability = the viability (from 0 to 100%) that Expert 2 assigned to the image

SAAVYTorch = the viability that SAAVY assigned to the analyzed image

CTG_viability = the viability (where appropriate matched data was available) that CTG 3D analysis output after normalization

CM

original_file = the original file name of the analyzed image (these were blinded before SAAVY analysis)

Image_Name = the filename that was assigned to the analyzed image during blinding

Treatment? = yes/no if the image was a well sample that was treated with gemcitabine on Day 4 of the associated experiment

np_c = the concentration of nanoparticles doped into the sample, where appropriate for noisy background study

Day = the day of the experiment (beginning at Day 0 for initial seeding) on which the image was captured

D0 ID = ground truth status for Day 0 spheroids, NaN if not Day 0 and 0 otherwise because insufficient time has passed to form spheroids

Expert 1 ID = based on the value that Expert 1 assigned to a sample when identifying the presence of spheroids. 0 for no spheroids and 1 for spheroids present

Expert 2 ID = based on the value that Expert 2 assigned to a sample when identifying the presence of spheroids. 0 for no spheroids and 1 for spheroids present

SAAVY ID = based on the value assigned to a sample based on SAAVY output, where no spheroids measured is a -1 output and otherwise is considered spheroid identified. 0 for no spheroids and 1 for spheroids present

CTG ID = the value assigned to a sample based on CTG output.

Expert 1 alive = based on the value that Expert 1 assigned to a sample when identifying if a spheroid was alive or dead. 0 for dead spheroids (viability of 0) and 1 for alive spheroids (spheroids with a viability greater than 0).

Expert 2 alive = based on the value that Expert 2 assigned to a sample when identifying if a spheroid was alive or dead. 0 for dead spheroids (viability of 0) and 1 for alive spheroids (spheroids with a viability greater than 0).

SAAVY alive = based on the value that SAAVY assigned to a sample when identifying if a spheroid was alive or dead. 0 for dead spheroids (viability of 0) and 1 for alive spheroids (spheroids with a viability greater than 0).

CTG alive = based on the value that CTG assigned to a sample when identifying if a spheroid was alive or dead. 0 for dead spheroids (viability of 0) and 1 for alive spheroids (spheroids with a viability greater than 0).

Software S1 (separate file).

All associated code is included on the GitHub: <https://github.com/armanilab/SAAVY>

SI References

1. W. Xiao, *et al.*, Matrix stiffness mediates pancreatic cancer chemoresistance through induction of exosome hypersecretion in a cancer associated fibroblasts-tumor organoid biomimetic model. *Matrix Biology Plus* **14**, 100111 (2022).
2. S. Ren, K. He, R. Girshick, J. Sun, Faster R-CNN: Towards Real-Time Object Detection with Region Proposal Networks. *arXiv* (2015) <https://doi.org/10.48550/arxiv.1506.01497>.
3. , `mwburke/population-stability-index`: Python implementation of the population stability index (PSI) (August 30, 2023).